Brazilian Journal of Chemical Engineering (2024) 41:851–863
https://doi.org/10.1007/s43153-023-00352-9

ORIGINAL PAPER

Syngas production via methane tri-reforming on Ni/La_2O_3–αAl_2O_3 catalysts

Vivian Vazquez Thyssen[1] · Ananda Vallezi Paladino Lino[2] · José Mansur Assaf[2] · Elisabete Moreira Assaf[3]

Received: 3 November 2022 / Revised: 5 May 2023 / Accepted: 12 May 2023 / Published online: 30 May 2023

Abstract

Ni/La_2O_3–αAl_2O_3 catalysts were characterized and tested in the methane tri-reforming reaction. The catalysts were prepared by the combustion method, and characterized by nitrogen physisorption, SEM, XRD, and *Rietveld* refinement, H_2-TPR, and CO_2-TPD. The metallic dispersion of Ni in the catalysts increased with the addition and increase of La_2O_3 amount. The reaction tests showed that the addition of La_2O_3, and the consequent increase in the metallic dispersion of Ni, influenced the catalytic results, favoring the selectivity towards H_2 production, leading to higher resistance to carbon deposition on the catalyst surface. However, there was a decrease in the selectivity towards H_2 and a higher rate of carbon deposition for catalysts with a higher additive content, having its maximum even with the increase in Ni dispersion, with the catalyst N10LαA. This result suggests that there was a limit for the La_2O_3 content, above which there would no longer be observed beneficial effects for the reforming process. The N2.5LαA catalyst showed the highest selectivity towards H_2 and the lowest carbon deposition rate among the catalysts.

Keywords Nickel · Lanthanum · Alpha-alumina · Catalyst · Methane tri-reforming

Introduction

The reliance on fossil fuels to meet energy demand has created serious environmental issues due to greenhouse gas (GHG) emissions. Methane (CH_4) is the most abundant GHG and the main contributor to recent climate changes, along with CO_2 (Abdullah et al. 2017).

Natural gas, the main source of CH_4, can be found associated or not with the oil. Its composition varies according to the location of its source. The average composition of Brazilian crude natural gas corresponds to 83% of CH_4, 0.9% CO_2, and other components such as ethane, propane, and hydrocarbons with four or more carbons (Agencia Iberoamericana para diffusion de la Ciencia y la Tecnologia 2020; GasNet 2020). In some Brazilian pre-salt deposits, the natural gas may have high levels of CO_2 (8–12 v/v%), which compromises the quality of the mixture and jeopardizes its employment in electricity generation in the power plants facilities of the oil platforms (GasNet 2020), as CO_2 diminishes the mixture average calorific power. According to the oil engineer Anelise Quintão Lara, CO_2 concentrations up to 40 v/v% were expected in the natural gas from Libra field production (Brasil Energia: Petróleo e Gás 2014).

The need to control global climate change, associated with its undesirable influence on the atmosphere, has generated great interest in converting natural gas into higher value-added fuels and petrochemicals. This ensures continuous energy sources and reduces the substantial dependence on crude oil (Abdullah et al. 2017).

The catalytic CH_4–CO_2 reforming combines two GHG to generate syngas ($CO + H_2$), which may subsequently be converted into clean liquid fuels. The dry reforming of CH_4 (DRM—Eq. 1) is, therefore, a promising reaction for the control of global warming. However, this process requires high energy consumption and presents the risk of carbon formation, because of the CH_4 decomposition (Eq. 2) and the

✉ Elisabete Moreira Assaf
eassaf@iqsc.usp.br

1 Centro de células a combustível, Instituto de Pesquisas Energéticas e Nucleares, Av. Prof. Lineu Prestes, 2242, Butantã, São Paulo, SP 05508-000, Brazil

2 Departamento de Engenharia Química, Universidade Federal de São Carlos, Rodovia Washington Luis, km 235, Jardim Guanabara, São Carlos, SP 13565-905, Brazil

3 Instituto de Química de São Carlos, Universidade de São Paulo, Av. Trabalhador São-Carlense, 400, São Carlos, SP 13560-970, Brazil

disproportionate CO produced throughout the *Boudouard* reaction (Eq. 3). The carbon deposition during the reaction may lead to the catalyst deactivation, which compromises the purity and the yield of the desired products, as well as the process stability (Song and Pan 2004).

$$CH_4 + CO_2 \leftrightarrows H_2 + 2CO \quad \Delta H_{298K} = +247\ kJ\ mol^{-1} \tag{1}$$

$$CH_4 \leftrightarrows C + 2H_2 \quad \Delta H_{298K} = +74\ kJ\ mol^{-1} \tag{2}$$

$$2CO \leftrightarrows C + 2CO_2 \quad \Delta H_{298K} = -171\ kJ\ mol^{-1} \tag{3}$$

To overcome the problems previously discussed, a new process, the methane tri-reforming (MTR), was proposed by Song and Pan (Song and Pan 2004). This process combines three reactions: dry reforming (Eq. 1), steam reforming (SRM—Eq. 4), and partial oxidation (POM—Eq. 5) of methane. In MTR, these reactions occur simultaneously in a single reactor. Furthermore, the MTR is often accompanied by the reverse water–gas shift reaction (RWGS—Eq. 6) (Osat and Shojaati 2022).

$$CH_4 + H_2O \leftrightarrows 3H_2 + CO \quad \Delta H_{298K} = +206\ kJ\ mol^{-1} \tag{4}$$

$$CH_4 + {}^1/_2O_2 \leftrightarrows 2H_2 + CO \quad \Delta H_{298K} = -30.6\ kJ\ mol^{-1} \tag{5}$$

$$H_2 + CO_2 \leftrightarrows CO + H_2O \quad \Delta H_{298K} = +41\ kJ\ mol^{-1} \tag{6}$$

By providing three oxidizing agents (CO_2, H_2O, and O_2), the MTR allows an improvement in the process stability, because it facilitates the removal of carbon (C) deposited on the catalytic material throughout the occurrence of C gasification reactions (Eqs. 7–9) (Chein et al. 2017).

$$H_2O + C \leftrightarrows CO + H_2 \quad \Delta H_{298K} = +131\ kJ\ mol^{-1} \tag{7}$$

$$CO_2 + C \leftrightarrows 2\,CO \quad \Delta H_{298K} = +171\ kJ\ mol^{-1} \tag{8}$$

$$O_2 + C \leftrightarrows CO_2 \quad \Delta H_{298K} = -394\ kJ\ mol^{-1} \tag{9}$$

The syngas H_2/CO ratio can be adjusted by manipulating the ratios of H_2O, O_2, and CO_2 relative to CH_4 as MTR reagents. This extends the syngas applicability, serving as a source of H_2 (directly applicable to fuel cells), as well as raw material for the synthesis of liquid fuels alternative to gasoline or diesel (Fischer–Tropsch synthesis—Eq. 10) (Jun et al. 2004; Kang et al. 2007; García-Vargas et al. 2014; Osat et al. 2022).

$$nCO + (2n+1)H_2 \leftrightarrows \left(-C_nH_{2n+2}-\right) + nH_2O \tag{10}$$

Ni supported on several materials presents appropriate activity and selectivity for syngas production via methane reforming. However, studies show that Ni deactivates rapidly, due to the carbon formation and/or sintering of the metal particles (Christensen et al. 2006). Researchers of the present group suggest that the performance of the Ni-based catalysts can be improved by using appropriate materials as catalyst support. In addition, the use of additives in the Ni catalysts can improve their catalytic performance in the reforming reactions, particularly concerning the metal–support interaction. Additives incorporation also contributes to minimizing the carbon deposition, due to the properties that facilitate the oxygen-adsorbed carbon species interaction, which accelerates the carbon oxidation to CO and/or CO_2 by their gasification (Eqs. 7–9) (Thyssen et al. 2013, 2015, 2017a, b; Thyssen and Assaf 2014).

The control of the $(CO_2 + H_2O + O_2)/CH_4$ ratios in the feed stream is also important to ensure the activity and stability of the catalyst, as reported by Świrk et al. (2020). Moreover, high CH_4 concentration in the feed compromises the stability of the catalyst, leading to C deposition, by the occurrence of methane decomposition (Eq. 2). Kumar and Pant (2020) reported that a balance between the catalyst basicity properties and the Ni^0 particle size led to a satisfactory performance along the MTR reaction, considering that one property was enhanced in exchange for another when studying Ni/Zn/Mg/Al hydrotalcite derived catalysts. Lino et al. (2020a) verified that the addition of Zr-Ce promoters with the Zr/Ce molar ratio of 0.25 on the $MgAl_2O_4$, which was used as the support for the Ni catalyst, improved the amount of basic sites, resulting in the enhancement of the CO_2 conversions along the MTR. Kumar et al. (2019) studied several materials as supports for the Ni-based catalysts applied to the MTR, such as Al_2O_3, SBA-15, TiO_2, ZrO_2, $(CeZr)O_2$, and MgO. According to these authors, the highest Ni dispersion, strongest nickel-support interaction, the highest degree of reducibility, and the most adequate amount of basic sites, ascribed to the Ni–Al_2O_3 catalyst, made it be selected as the most suitable material for the MTR.

The applicability of α-Al_2O_3 (corundum) as catalyst support is mainly due to its characteristics such as high electrical resistance, and thermal, chemical, and mechanical stability. Besides, it is considered a low-cost material, which facilitates a large-scale application (Li et al. 2005; Alsaffar et al. 2021).

Among the additives, the incorporation of La_2O_3 to the support usually increases the Ni dispersion on the surface, which may hinder carbon deposition during the reaction and facilitate its gasification (Cui et al. 2007; Gao et al. 2008). Moreover, La_2O_3 improves the active phase dispersion and leads to the formation of lanthanum oxycarbonate ($La_2O_2CO_3$) species, as La_2O_3 reacts with CO_2, which further oxidizes the surface carbon (C), restoring the La_2O_3

species and producing CO (Song et al. 2017). These features are of extreme importance for methane-reforming reactions. The presence of La_2O_3 in the Ni/SiO_2 catalyst diminished the amount of coke deposition along the reforming of acetic acid with water steam, due to the enhancement of the metal–support interaction and small particle size (Guo et al. 2022). The increment of the amounts of basic sites, due to the La addition in Co–Ru/MgO–Al_2O_3 catalyst, was responsible for the increment of the CO_2 conversion and minor carbon formation in the MTR; in addition, the better performance of La-containing catalyst compared to the unpromoted material was also explained by the presence of $La_2O_2CO_3$ species, that facilitates the carbon gasification, as commented previously (Kumar et al. 2021).

Taking into consideration what was discussed previously, the objective of this study was: (i) preparation of Ni/La_2O_3–αAl_2O_3 catalysts with different concentrations of La_2O_3; (ii) characterization of the catalysts for a better understanding of their properties, and (iii) evaluation of the influence of the La_2O_3 concentration on the catalyst performance in syngas production in MTR. Even though αAl_2O_3 is a support for Ni-based catalysts vastly applied to the methane reforming reactions (Pompeo et al. 2007, 2009; Cichy et al. 2022), a study evaluating the effects relative to the lanthanum incorporation in the $Ni/\alpha Al_2O_3$ catalyst on methane tri-reforming reaction were not reported yet, to the best of the authors' knowledge.

Experimental

Preparation

Techniques of combustion for material synthesis are interesting due to their fast, economical, and energy-efficient process (Kumar et al. 2011). Therefore, our catalysts were prepared by the combustion method, following the procedure detailed in Vilela et al. (2021). The materials were named: αA, NαA, N2.5LαA, N5LαA, and N10LαA; for commercial α-Al_2O_3, 10 wt% of Ni on commercial α-Al_2O_3, 10 wt% of Ni and 2.5 wt% of La_2O_3 on commercial α-Al_2O_3, 10 wt% of Ni and 5.0 wt% of La_2O_3 on commercial α-Al_2O_3, and 10 wt% of Ni and 10.0 wt% of La_2O_3 on commercial α-Al_2O_3, respectively.

The first step of the process was to stir a solution with a small volume of water for homogenization of the components: commercial α-Al_2O_3, $La(NO_3)_3.6H_2O$, $Ni(NO_3)_2.6H_2O$, and urea—all in stoichiometric proportions to obtain the final catalyst (Table 1). This was followed by combustion at 400 °C and heat treatment at 750 °C under synthetic airflow. Both nitrates functioned as an oxidizer of the reaction, and urea was the fuel.

Characterization

Surface-specific areas of the samples were determined in a Quantachrome Nova 1000e instrument, by N_2 physisorption (B.E.T. method).

Scanning electron microscopic (SEM) analyses were performed under an LEO-440 scanning electron microscope equipped with an Oxford detector to visualize the morphology of the catalysts, before, and after reactions.

The samples were characterized by X-ray diffraction (XRD) for the identification of the crystalline phases. XRD analyses were performed on a Bruker diffractometer (D8 Advance). The crystalline phases were identified by the Crystallographica Search Match software, and all the diffractograms were refined by the *Rietveld* method using TOPAS® (Bruker AXS) Software Version 5.

H_2 temperature-programmed reduction (H_2-TPR) was carried out in an Analytical Multipurpose System (SAMP3) to assess the reducible species present in the catalysts. By the reduction profiles, the degree of sample reduction in the activation temperature was calculated.

CO_2-TPD analyses were carried out in Micromeritcs Autochem II equipment to estimate the basicity properties of the materials.

Samples reduced under the activation conditions were analyzed by XRD to estimate the average size of Ni^0 by TOPAS® (Bruker AXS) Software Version 5.

Metal dispersion D_M (%) was estimated from the average crystallite size of Ni^0, dNi^0 (nm), by Eq. (11), considering spherical-shaped particles (Bartholomew and Farrauto 2006):

Table 1 Amount (g) of reagents to produce 1 g of material

Catalysts	Commercial α-Al_2O_3	$Ni(NO_3)_2{\cdot}6H_2O$	$La(NO_3)_3{\cdot}6H_2O$	Urea	H_2O
αA	1	–	–	–	–
NαA	0.90	0.50	–	0.17	5 mL
N2.5LαA	0.88	0.50	0.03	0.18	5 mL
N5LαA	0.86	0.50	0.06	0.19	5 mL
N10LαA	0.81	0.50	0.12	0.21	5 mL

$$D_M = 101.2 / dNi^0 \quad (11)$$

Catalytic evaluation

Before the reaction, the samples were activated in situ for 30 min under H_2 flow at 750 °C. Tests were performed in a tubular quartz reactor fed with CH_4:CO_2:H_2O:O_2:N_2 in a molar ratio of 1:0.33:0.33:0.17:0.68 (stoichiometric ratio of MTR), maintaining a spatial velocity of 45,000 NmL(g_{cat} h)$^{-1}$. For each reaction, 200 mg of sieved catalyst (60–100 mesh) was used. The tests were performed at 700 °C (Świrk et al. 2020) for 4 h at atmospheric pressure. The N2.5LαA catalyst was also tested for 12 h at the same reaction conditions.

A gas chromatograph (VARIAN GC-3800), equipped with two Porapak-N® columns and with a Molecular Sieve 13X, and two TCDs, was used in-line for the analysis of the gaseous products reaction.

The performances of the catalysts were evaluated in terms of the CH_4 (X_{CH_4}) and CO_2 (X_{CO_2}) conversions, and H_2 (Y_{H_2}) and CO (Y_{CO}) yields, using the following expressions:

$$X_{CH_4} = \frac{F_{CH_4\ in} - F_{CH_4\ out}}{F_{CH_4\ in}} \times 100\% \quad (12)$$

$$X_{CO_2} = \frac{F_{CO_2\ in} - F_{CO_2\ out}}{F_{CO_2\ in}} \times 100\% \quad (13)$$

$$Y_{H_2} = \frac{F_{H_2\ out}}{2F_{CH_4\ in} + F_{H_2O\ in}} \times 100\% \quad (14)$$

$$Y_{CO} = \frac{F_{CO\ out}}{F_{CH_4\ in} + F_{CO_2\ in}} \times 100\% \quad (15)$$

where $F_{i\ in/out}$ represents the molar flow of "*i*" ($i = CH_4$, CO_2, H_2O, H_2 or CO) that enters (*in*), or leaves (*out*) the reactor.

The turnover frequencies (TOF) were estimated considering the rates of CH_4 and CO_2 converted, per unit of Ni^0:

$$TOF_i = \frac{X_i \cdot F_{i,\ in}}{C_{Ni} \cdot \frac{m_{cat}}{MM_{Ni}} \cdot D_M} \quad (16)$$

where "*i*" represents CH_4 or CO_2, X_i is the percent conversion of CH_4 or CO_2, $F_{i,in}$ is the molar rate of CH_4 or CO_2 that was fed to the reactor, C_{Ni} is the nickel weight concentration in the catalysts (0.10), m*cat* is the weight of the catalyst loaded inside the reactor (200 mg), MM_{Ni} is the molar weight of nickel, and D_M is the metallic dispersion (%) of the Ni^0 particles in the reduced catalysts (before reaction—B) or after the MTR reaction (post-reaction—A), estimated according to Eq. (11).

Similarly, the production of H_2 and CO (P_i) per unit of Ni^0 available on the catalyst surface was calculated according to Eq. (17):

$$P_i = \frac{F_{i,\ out}}{C_{Ni} \cdot \frac{m_{cat}}{MM_{Ni}} \cdot D_M} \quad (17)$$

where "*i*" represents H_2 or CO, and $F_{i,out}$ is the molar rate of H_2 or CO in the effluent stream.

A ThermoScientific (FlashSmart) Elemental Analyzer equipment determined the amounts of carbon (coke) formed during the reaction.

The spent catalysts were also characterized by XRD to estimate the average size of Ni^0 crystallite and the phase quantification by *Rietveld* refinement using TOPAS® (Bruker AXS) Software Version 5. ^{27}Al-NMR experiments were performed in a Bruker 400 MSL instrument to verify the presence of pentacoordinate Al species in the spent catalysts, ascribed to the formation of the $LaAlO_3$ phase.

Results and discussion

Characterization

Table 2 shows small values for the surface areas of the samples, as expected for α-Al_2O_3-based materials (Kumar et al. 2011). There was also a decrease in the value of this parameter, with the addition of La and Ni in the α-Al_2O_3 support, that followed the increase of the additive content, which, despite being within the intrinsic error of the measurement, followed the tendency, found in the literature (Kumar et al. 2011; Habibi et al. 2014; Kalai et al. 2018). This decrease may be related to the possible particle agglomeration on the surface during sample preparation (Thyssen et al. 2013, 2015, 2017a, b; Thyssen and Assaf 2014).

Figure 1 shows the XRD patterns of the fresh catalysts. All samples exhibited intense peaks related to the α-Al_2O_3 phase (α—PDF 82-1467). NiO peaks (n—PDF 47-1049) were identified with lower intensity. With the addition of La_2O_3, these peaks were less intense, suggesting an increase in NiO dispersion in the catalyst. The most intense NiO peak would be approximately 43°, which overlaps with the α-Al_2O_3 peaks. A broad peak with low intensity, related to the $LaAlO_3$ phase (la—PDF 82-478), could be noticed for the N10LαA fresh catalyst. With the phase quantification using the *Rietveld* refinement, the $LaAlO_3$ phase appeared in small concentrations in the catalyst with the lowest La_2O_3 content (N2.5LαA). La_2O_3 peaks may be absent because they are low in intensity and close to the α-Al_2O_3 peaks,

Table 2 α-Al_2O_3 and fresh catalysts specific surface areas (S—$m^2\ g^{-1}$); phase quantification by *Rietveld* refinement (wt%); Ni^0 crystallite average size (dNi^0—nm)[a], metallic dispersion (D_M—%)[a], and contribution (%) of the H_2 consumption upon the reduction of Ni(II) species with distinct strength of interaction with the α-Al_2O_3[a]

Samples	S	Phases quantification			dNi^0	D_M	Weak interaction (350–500 °C)	Moderate to strong interaction (> 500 °C)
		α-Al_2O_3	$LaAlO_3$	NiO				
αA	10.1	100	–	–	–	–	–	–
NαA	4.2	88.5	–	11.5	48.6	2	84	16
N2.5LαA	2.7	88.7	0.3	11.0	39.4	3	67	33
N5LαA	2.2	86.9	1.5	11.6	32.5	3	54	46
N10LαA	2.0	84.8	4.2	11.0	25.4	4	60	40

[a]Determined after reduction with H_2

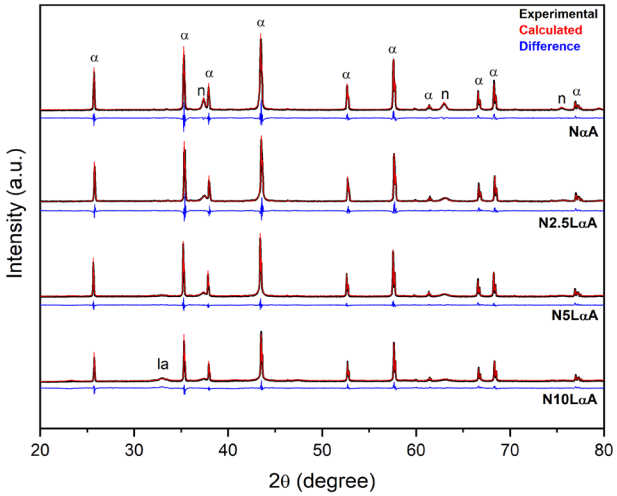

Fig. 1 XRD patterns of the fresh catalysts. α-Al_2O_3 (α—PDF 82-1467); NiO (n—PDF 47-1049); $LaAlO_3$ (la—PDF 82-478)

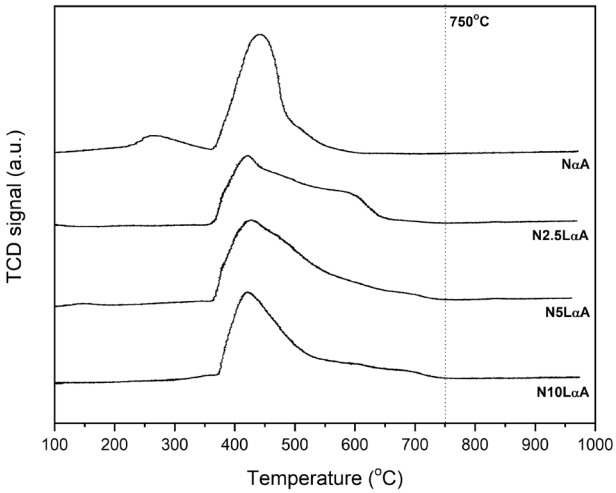

Fig. 2 H_2-TPR of the catalysts

which does not mean that the former phase is not present in the mixed catalysts.

Figure 2 shows the reduction profile of the catalysts. Peaks in the range of 200–300 °C are present in the profile of NαA catalyst, and it was attributed to the surface oxygen reduction (Damyanova et al. 2002). Peaks at a temperature higher than 300 °C were ascribed to the reduction of Ni(II) species ($Ni^{2+} \rightarrow Ni^0$), which develop several types of interaction with the support: (i) between 300 and 500 °C, they can be attributed to the Ni(II) species with weak support interaction, such as free NiO species, and (ii) above 500 °C, they refer to the activation of the Ni(II) with a moderate/strong interaction with the support (Gao et al. 2008; Guo et al. 2022).

It was observed that the H_2 consumption ends at higher temperatures as the La content increases, reaching approximately 750 °C for the N10LαA catalyst. This fact suggests an increase in the Ni(II) interaction with the modified materials, and an increase in the Ni dispersion on the catalyst surface (Thyssen et al. 2017a). The dispersion of the Ni^0 particles produced after the H_2 activation at 750 °C increased with the La_2O_3 content, as shown in Table 2, confirming that the addition of La_2O_3 resulted in smaller metallic particles.

Table 2 also shows the contribution (%) of each temperature zone related to the activation of the Ni(II) species, obtained from the deconvolution of the H_2 consumption curves shown previously. In the case of the NαA catalyst, most of the Ni(II) species interacted weakly with alumina, considering that 84% of the H_2 consumption ascribed to the reduction of Ni^{+2} to Ni^0 ranges from 350 to 500 °C, as summarized in Table 2. There was also an increment of the H_2 consumption contribution, which was related to the reduction of Ni(II) species which developed moderate to strong interaction with the α-Al_2O_3 (temperature > 500 °C), as the amount of La_2O_3 increases, according to the previously discussed. The addition of La_2O_3 in the γ-Al_2O_3 facilitates the reduction of Ni(II) at lower temperatures, by diminishing the interaction of the nickel species with alumina and increasing the interaction with the La additive, resulting in higher

reducibility at lower temperatures (Anjaneyulu et al. 2013). The results in this present work show that this did not occur in the case of the α-Al_2O_3, because the amount of reduced species at lower temperatures decreased (Table 2), which suggests an increased interaction of the Ni(II) with the support. In the case of γ-Al_2O_3, which has a high surface area (~ 220 m^2/g), $NiAl_2O_4$ species are formed, being reduced at elevated temperatures (above 800 °C) (Thyssen et al. 2015; Tsiotsias et al. 2021). By using α-Al_2O_3 as the support, it was observed that the Ni(II) present in the sample did not form an aluminate phase, being more easily reduced at lower temperatures.

The average crystallite size of Ni^0 was obtained with TOPAS® software, using the ex-situ XRD patterns (Fig. 3) of the catalysts, which were reduced at 750 °C (activation temperature of the material). The results are shown in Table 2, as well as the metallic dispersion of the catalysts estimated from the average Ni^0 crystallite size, according to Eq. (11).

The values of metallic dispersion increased with the La concentration, according to (Table 2). Ni(II) species, with a strong interaction with the support, produced more dispersed Ni^0 particles, which were formed during the activation process before the reaction, while disadvantaging the sintering process that could occur on the material surface along the reaction, leading to the catalyst deactivation (Thyssen et al. 2017a). Both XRD and TPR analyses agreed with these data, since the intensity of the NiO peaks in diffractograms decreased with increasing the La_2O_3 content (XRD), and Ni(II) reduction temperature increased (TPR), already suggested a higher Ni dispersion in the material.

CO_2 desorption curves are represented in Fig. 4. According to Al-Mubaddel et al. (2021), the basic sites of both weak and moderate strength were related to the peaks up to

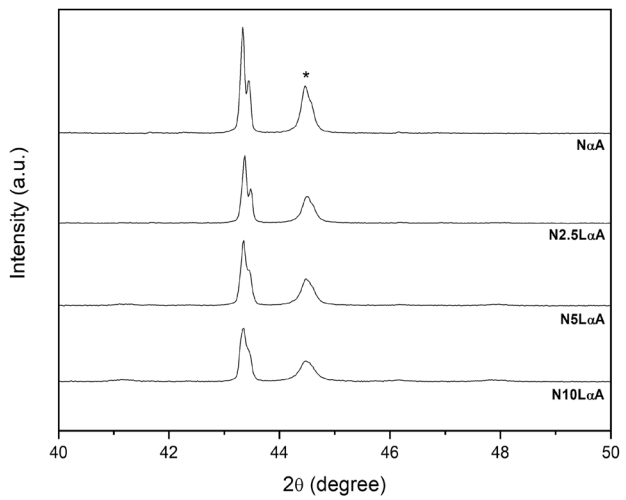

Fig. 3 XRD—samples activated at 750 °C. Ni^0 (*—PDF 89-7128)

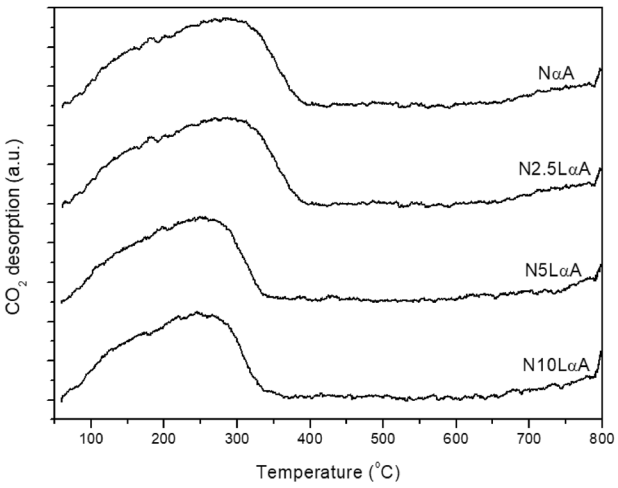

Fig. 4 CO_2-TPD of the reduced catalysts

200 °C, as the strong basic sites, ascribed to the CO_2 adsorption on the isolated O^{-2} species, were related to the peaks at the temperature range of 200–400 °C. Super strong basic sites may be related to the CO_2 adsorption as unidentate carbonate, at temperatures superior to 500 °C (Song et al. 2017; Al-Mubaddel et al. 2021). As observed in Fig. 4, these last types of sites were not present in the samples reported in this present work. Moreover, the main peak ascribed to the CO_2 desorption (250–300 °C) shifted to a lower temperature with the La_2O_3 addition, and the content increased from 2.5 to 5 wt%.

The curves shown in Fig. 4 were deconvoluted to verify the contribution of each type of basic site, to classify them according to their strength, and to estimate the total basicity. This information is summarized in Table 3. The total basicity and the amount of strong basic sites diminished with the La_2O_3 addition, and with the increase of the additive content. The decrease of the amounts of basic sites with lanthanum addition was also reported by Al-Mubaddel et al. (2021) after incorporating 10 wt% of La_2O_3 in Ni/γ-Al_2O_3 catalyst, as a consequence of the disappearance of the bidentate carbonate species (moderate strength basic sites); the basic sites were greatly nurtured only with the addition of 15 wt% of lanthanum in the catalyst. According to Table 2, the specific surface areas of the fresh catalysts diminished with the

Table 3 Basicity properties of the catalysts (μmol g^{-1})

Catalysts	Weak-moderate sites	Strong sites	Total basicity
NαA	26	120	146
N2.5LαA	29	107	136
N5LαA	14	88	102
N10LαA	25	81	106

La addition; such a trend may be extended to the reduced catalysts, which could lead to lower amounts of basic sites available for CO_2 adsorption.

Catalytic evaluation

Table 4 shows the average conversions of CH_4 and CO_2 (calculated according to Eqs. 13 and 14), considering the average values along the 4 h of TOS, average H_2/CO ratios, and the average H_2 and CO yield CO_2 (calculated according to Eqs. 15 and 16), as well as the carbon deposition rate during the reaction.

O_2 is a highly reactive oxidant, which was completely converted for all catalysts. Except for the N10LαA catalyst, the average reagent conversions were similar among the samples, as shown in Table 4. Therefore, for a better comparison among the samples evaluated under MTR conditions, the turnover frequencies of both CH_4 and CO_2 are shown along the time on stream (TOS), calculated according to Eq. (16). The reagents were probably converted under distinct rates for each material because the dispersion of the Ni^0 particles estimated after the activation process presented different values for each catalyst, as shown in Table 2. The conversion rates of the reagents (CH_4 and CO_2) per unit of Ni^0 available on the catalyst surface were plotted with TOS, as shown in Fig. 5. Figure 6 shows the production of H_2 and CO per unit of Ni^0 available on the catalyst surface plotted with TOS, supposing that no meaningful sintering of the metallic phase occurred.

The TOF of CH_4 decreased with the La_2O_3 addition and with the increase of the additive concentration in the catalysts; as for the CO_2, it remained similar for all catalysts (Fig. 5). The methane conversion values were similar for all the materials (Table 4) and the dispersion of the active phase increased as lanthanum was incorporated into the catalysts, according to Table 2. This suggests that the CH_4 conversion rate per unit of the exposed active phase in the catalyst surface (TOF of CH) was different among the catalysts, and it diminished with the promoter incorporation. The TOF values for the CO_2 were almost the same for all the catalysts once the values ascribed to the surface

Table 4 MTR results: average conversions (%), average H_2/CO molar ratio, average products yields (%), and carbon deposition rate (C—mgC (gcat h)$^{-1}$) in a 4 h-reaction at 700 °C; average CH_4 turnover frequencies at the beginning of the reaction (B) and after reaction (A) ($-\times10^3$ molCH$_4$ mol$_{Ni}^{-1}$ h^{-1}); quantification of $La_2O_2CO_3$ and C phases using *Rietveld* refinement (wt%) and Ni^0 average crystallite size (dNi^0_{pr}—nm) and metallic dispersion (D_{Mpr}—%) of the post-reaction catalysts

Samples	Average conversions and average H_2/CO			Yields		TOF CH_4		C	Phases			dNi^0_{pr}	D_{Mpr}
	CH_4	CO_2	H_2/CO	H_2	CO	B[a]	A[a]		C_{graf}	$LaAlO_3$	$La_2O_2CO_3$		
NαA	44.2	22.5	1.8	59	58	11	10	30	2.3	–	–	47.1	2
N2.5LαA	46.3	23.6	1.9	72	68	9	11	24	2.8	0.8	0.02	42.9	2
N5LαA	45.0	20.9	1.8	67	66	7	7	28	4.1	1.8	0.09	34.8	3
N10LαA	56.7	40.1	1.7	69	70	7	8	41	5.6	2.9	0.05	26.4	4

[a]Values estimated considering the metallic dispersion of the Ni^0, at the beginning of MTR, considering the dispersion of the reduced catalyst (B), and after 4 h on stream, considering the dispersion of the spent catalyst (A)

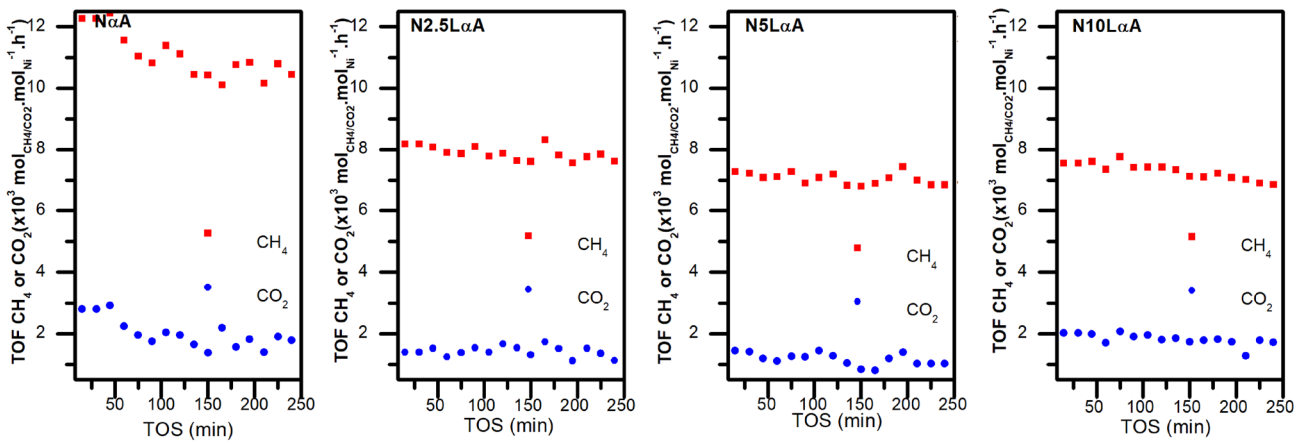

Fig. 5 TOF* during MTR at 700 °C. * calculated according to Eq. (16)

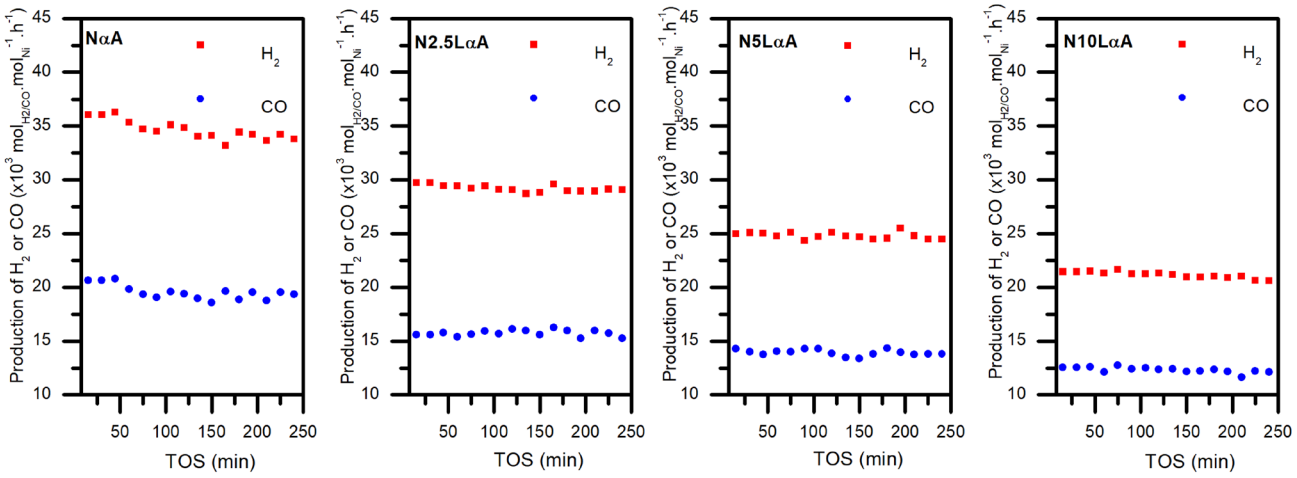

Fig. 6 Production* of H_2 and CO per mol of exposed Ni^0 on the surface of the catalyst during MTR at 700 °C. * calculated according to Eq. (17)

basicity diminished with La addition, despite the increment of the active phase dispersion. Increasing the La_2O_3 concentrations from 2.5 to 10 wt% caused the H_2 and CO productions to decrease expressively, as shown in Fig. 6, because of the decrease of CH_4 TOF. As the CO production per mol of Ni^0 exposed on the surface diminished with both N5LαA and N10LαA (Fig. 6), it may be inferred that the *Boudouard* reaction (Eq. 3) showed greater participation for these catalysts, compared to both NαA and N2.5LαA samples. This could explain the fact that the carbon deposition rate decreased with the La_2O_3 addition to 2.5 wt% in the catalyst, but then it increased with its concentration, reaching 41 mC $(gcat\ h)^{-1}$ for N10LαA catalyst.

The values of TOF were greater than the values reported in some other works. Świrk et al. (2020) reported TOF of CH_4 values ranging from 13×10^{-2} to 75×10^{-2} s^{-1}, at 700 °C, for Ni/Mg/Al derived hydrotalcite's catalyst; Izquierdo et al. (2014) evaluated Ni/Ce–Al_2O_3, Ni/Ce–Zr–Al_2O_3, and Ni–Rh/Ce–Zr–Al_2O_3 catalysts during MTR and the TOF of CH_4 values ranged from 3×10^{-2} to 5×10^{-2} s^{-1}. Nonetheless, the TOF of CH_4 reported in this present work ranged from 7.3×10^3 to 11×10^3 $mol_{CH4}\ mol_{Ni}^{-1}\ h^{-1}$ (2 to 3 $mol_{CH4}\ mol_{Ni}^{-1}\ s^{-1}$), and they were comparable to the values observed by Özdemir et al. (2014), for the Ni/$MgAl_2O_4$ catalyst, whose TOF of CH_4 values ranged from 7 to 37 $mol_{CH4}\ mol_{Ni}^{-1}\ s^{-1}$, in the partial oxidation of methane reaction. They were also comparable to the values reported by Gupta and Deo (2023), during the methane tri-reforming reaction, using Ni-based catalysts supported on γ-Al_2O_3, for which the TOF values ascribed for CH_4 ranged from 0.31 to 1.61 $mol_{CH4}\ mol_{Ni}^{-1}\ s^{-1}$. According to Fig. 5, the average TOF values for CO_2 varied from 1.2×10^3 to 2×10^3 $mol_{CO2}\ mol_{Ni}^{-1}\ h^{-1}$ (0.33–0.55 $mol_{CO2}\ mol_{Ni}^{-1}\ s^{-1}$), which are in the same order of magnitude as the TOF values for CO_2, also reported by Gupta and Deo (2023), that ranged from 0.07 to 0.23 $mol_{CO2}\ mol_{Ni}^{-1}\ s^{-1}$.

Majewski and Wood (2014) evaluated a Ni/SiO_2 (11 wt%) catalyst at 650 °C, using a feed ratio condition of $1CH_4{:}0.5CO_2{:}0.5H_2O{:}0.1O_2$, and reported that the carbon deposition was equivalent of 49 mC $gcat^{-1}$ for a TOS of 4 h, i.e. 2.25 mgC $(g_{cat}\ h)^{-1}$, which is smaller than the amount of the carbon deposits found on the surface of the N2.5LαA catalyst; despite the low temperature of the reaction (650 °C), the condition adopted by those authors could be considered milder than the stoichiometric MTR condition used in this present work, since in the former case the gasifying agents CO_2 and H_2O were in excess relative to CH_4, allowing a better carbon gasification environment.

When simulating a biogas feed composition for MTR ($1CH_4{:}0.67CO_2{:}0.3H_2O{:}0.1O_2$) at 800 °C, Vita et al. (2014) found that the carbon deposition rate ascribed to the Ni/CeO_2 (7.7 wt%) catalyst was 110 mgC $(gcat\ h)^{-1}$, which was more than four times superior than the amount of carbon deposits on the N2.5LαA catalyst. As the main reactions responsible for the carbon deposition, represented by Eq. (3) and by the reverse of the reaction shown in Eq. (7), are usually favored at lower temperatures, the condition adopted for the evaluation of the catalysts reported in the present work would be more prone to the formation of carbon deposits than the temperature adopted by those authors.

The average H_2/CO molar ratios were found to be close to the value expected for the stoichiometric MTR condition, where H_2/CO would be 1.75. The N2.5LαA catalyst featured the highest average H_2/CO molar ratio, as shown in Table 4, and this would be ascribed to greater participation of the SRM (Eq. 4), which is responsible to generate a more H_2-enriched syngas (Lino et al. 2020b). Syngas with an H_2/CO ratio ranging from 1.5 to 2.0 can be used in the *Fischer–Tropsch* process, for methanol production, and

dimethyl ether synthesis, according to the reaction represented by Eq. (10) (Farniaei et al. 2014).

The improvement of the average H_2 and CO yields and the decrease in the rate of the carbon deposition (Table 4) for the N2.5LαA catalyst could be explained by the increase in the Ni dispersion with the La_2O_3 addition in the material. However, it is observed that even though this dispersion was greater for the catalysts with higher content of additive (5 and 10 wt%) (Table 2), there was a change in the catalyst performance, with a decrease in the H_2 and CO production (Fig. 6), and an increase in the rate of carbon deposition. As shown in Table 3, the total basicity and the amount of strong basic sites decreased meaningfully for both N5LαA and N10LαA catalysts. Such a fact negatively influenced the performances of these two catalysts towards the MTR, leading to higher carbon deposition rates, hence compromising the syngas production. This showed that the active phase dispersion is not the only parameter that influences the carbon deposition, but also the total basicity properties (Lino et al. 2019).

According to Świrk et al. (2020), changes in the crystallite size of the metallic particles are usually related to TOF, and this value increased with the crystallite size of the particle. They also reported that an increase in the TOF values for methane along the reaction, i.e., TOF of CH_4 after reaction (A) being higher than TOF of CH_4 at the beginning of the reaction (B), evidenced the sintering of the catalyst and the loss of metallic area, leading to the accumulation of the carbon during the MTR. The present study did not follow such a trend, as the N2.5LαA featured the highest average TOF values, both at the beginning of the reaction (B) and after 4 h on stream (A), but the lowest carbon deposition, as the opposite was observed with both N5LαA and N10LαA (Table 4). In this case, other catalytic properties, such as the basicity features, discussed previously, instead of the metallic dispersion, could explain the accumulation of the carbon species, mainly on the surface of the catalyst containing the highest La_2O_3 concentration.

Literature studies (Thyssen et al. 2017b; Kumar et al. 2021; Bertoldi et al. 2022) showed that the La_2O_3 addition in the catalytic materials facilitates the gasification of the carbon species by the formation of La_2O_3 carbonate, through the reactions represented by Eqs. (18) and (19). Part of the CO_2 in the catalytic system will react with La_2O_3 and form oxycarbonate species (Eq. 18), which would react with the carbon adsorbed on Ni sites, releasing it as CO (Eq. 19).

$$CO_2 + La_2O_3 \leftrightarrows La_2O_2CO_3 \quad (18)$$

$$La_2O_2CO_3 + C \leftrightarrows La_2O_3 + 2CO \quad (19)$$

To be available for the reaction with the CO_2, lanthanum must be found as La_2O_3 phase to produce the carbonate species, according to Eq. (18), followed by the gasification of carbon deposits, according to Eq. (19). The diffractograms of the fresh catalysts showed the formation of $LaAlO_3$ phase (Table 1) instead of the La_2O_3 with the increase of the additive content. The former phase is less prone to react with CO_2 compared to the La_2O_3 phase, hence the carbon gasification through the carbonate species is hindered. The unavailability of La species as La_2O_3, due to the formation of the $LaAlO_3$ phase, may also affect the alkalinity properties discussed earlier. That is because the former oxide would be responsible for the uptake of CO_2, producing an intermediate product (carbonate) responsible for carbon gasification. This also explains the increase in the carbon deposits with increasing additive content in the material (Table 4).

The $LaAlO_3$ phase was already observed with 2.5 wt% of La_2O_3 in the spent catalysts (Table 4), and the peaks ascribed to this phase became more intense as the concentration of the additive increased in these samples, as shown in the XRD of the spent catalysts (Fig. 7). As for the fresh catalyst, this phase only appeared clearly for the N10LαA sample (Fig. 1). This suggests that the reaction conditions modified the catalyst structure, enhancing the formation of $LaAlO_3$ species.

The ^{27}Al nuclear magnetic resonance (NMR) also evidenced the transformation of the phases during the reaction through the changes in the aluminum coordination (Fig. 8). In the fresh catalysts, the main Al coordination in the α-Al_2O_3 was ascribed to the octahedral (Al^{VI}) coordination, i.e., saturated Al sites. After the reaction, the band became a little asymmetric, and at around 35 ppm, especially for the N10LαA catalyst, a small band appeared, relative to the presence of the pentacoordinate Al sites (Al^{V}), ascribed to the formation of Al-O-La links in the $LaAlO_3$ phase (Shi

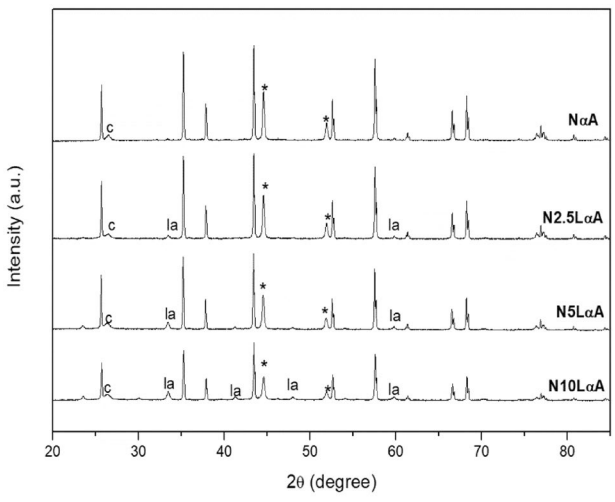

Fig. 7 XRD patterns of spent catalysts. C (carbon deposits), *(Ni^0), la ($LaAlO_3$)

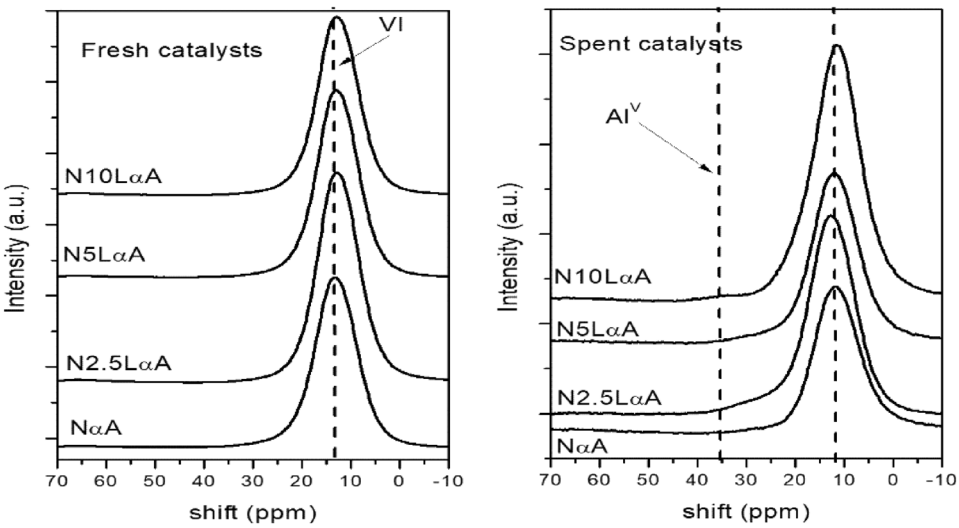

Fig. 8 ^{27}Al-NMR of the fresh and spent catalysts

et al. 2015; Song et al. 2017). This result corroborates with the increment of the $LaAlO_3$ phase concentration, estimated by *Rietveld* refinement (Table 4), as the La_2O_3 concentration in the catalysts increased from 2.5 to 10 wt%.

The SEM images of N2.5LαA and N10LαA catalysts, which had the lowest and highest rate of carbon deposition in the reaction, respectively, are shown in Fig. 9. The micrographs allowed the comparison of morphology and observation of deposited coke during the reaction.

By comparing the images of the catalysts before and after the tests, the formation of coke deposits throughout the MTR was observed. With the Ni-based catalysts, the formation of filamentous carbon is expected, in which the C formed during the reaction is deposited at the support/Ni active phase interface, forming a filament separating the metallic Ni and support. The formation of this filament could cause catalyst deactivation, due to the loss of the active phase, which happens with the rupture of the particles caused by the carbon diffusion through the crystallites (Trimm 1999; Thyssen et al. 2019). SEM images of post-MTR catalysts confirmed the formation of this type of carbon, as expected for the catalysts with Ni as the active phase.

By comparing the images of the post-MTR catalysts, a greater deposit of filaments was observed with the highest content of additive, as discussed previously, and shown in Table 4.

Among the catalysts studied in this present work, the N2.5LαA was considered the best, because it diminished the carbon formation and yielded more H_2 and CO as desired products (Table 4). Thus, this catalyst was selected for a 12 h time on stream reaction. Figure 10 shows the N2.5LαA catalyst performance along the 12 h-MTR test. According to the elemental analysis, the amount of the carbon deposited after this 12 h-stability test, about 51 mgC $(g_{cat}\ h)^{-1}$, was 24% greater than the short-time stability test (TOS = 4 h). Kumar and Pant (2020) observed a loss of activity from 100 min of TOS, along a stability test of 20 h, ascribed to the sintering of the active phase and to the deposition of carbon, which was reported to be 1 mgC $gcat^{-1}\ h^{-1}$, with a hydrotalcite-derived Ni–Zn–Mg–Al catalyst (2.5% wt Ni loading) applied to the methane tri-reforming reaction. The relatively high amount of carbon deposits on the N2.5LαA catalyst could also explain its deactivation, as the methane and carbon dioxide conversions decreased (Fig. 10a), as well as the products yields (Fig. 10b), especially noticed after 3 h of TOS.

Conclusions

It was concluded that the addition of La_2O_3 in the NαA catalyst increased the dispersion of Ni on the catalyst surface, despite diminishing the total catalyst basicity. With the reaction tests, it was observed that the addition of La_2O_3 and the consequent increase in the metallic dispersion of Ni affected the catalytic results: the selectivity towards H_2 was favored and the carbon deposition on the surface of the catalyst was decreased. However, even with the increase in Ni dispersion, for catalysts with a higher additive content, there was a drop in selectivity in H_2 and a higher rate of carbon deposit, having its maximum with the catalyst N10LαA, due to the decrease of both total basicity and amounts of basic sites of strong strength. This would be also related to the difficulty in forming $La_2O_2CO_3$, produced by the CO_2 adsorption on the La_2O_3. The carbonate species assist in the gasification of C, and its formation was compromised when La_2O_3 was inaccessible due to the formation of the $LaAlO_3$ phase. These results showed that there was a limit to the La_2O_3 content in α-Al_2O_3-based catalysts, above which there were no longer beneficial effects for the catalytic process. The catalyst with

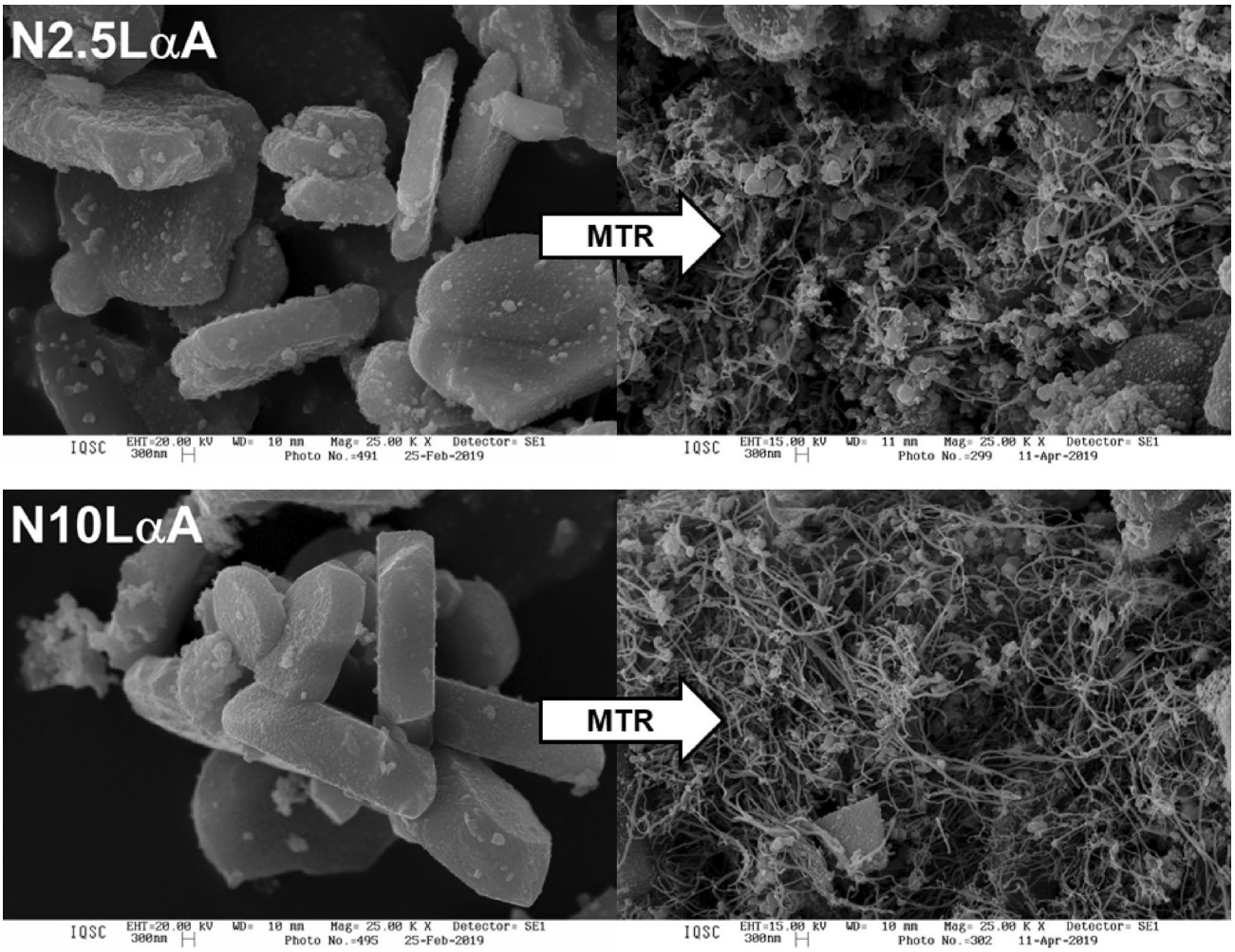

Fig. 9 SEM of N2.5LαA and N10LαA post-reaction catalysts

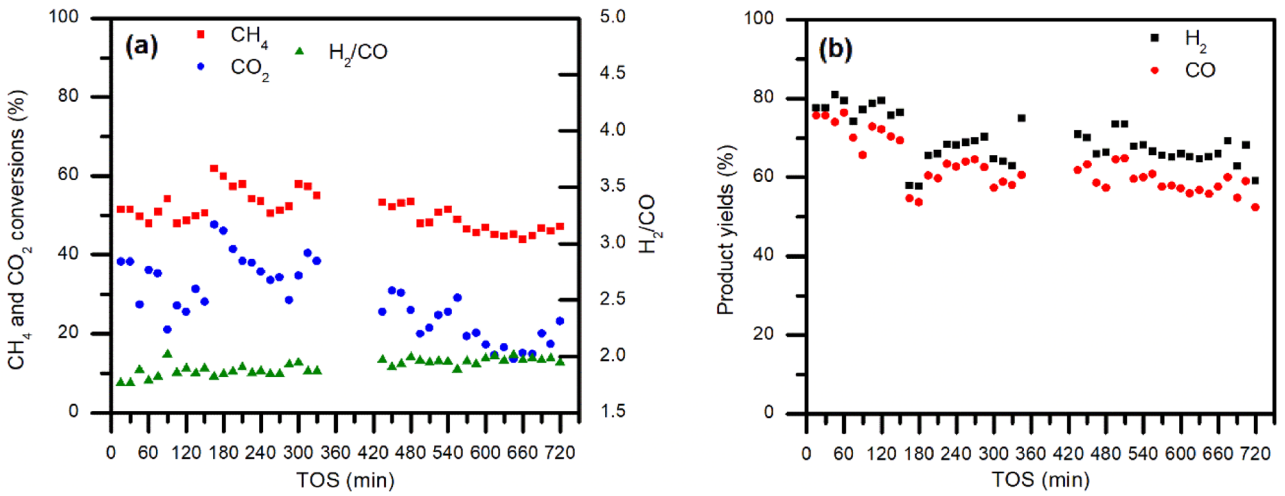

Fig. 10 N2.5LαA—12 h MTR: **a** CH_4 and CO_2 conversions and H_2/CO ratios; **b** H_2 and CO yields

the lowest La content, N2.5LαA, was the one with the highest selectivity towards H_2 and the lowest carbon deposition.

Acknowledgements CNPq (304883/2016-6), CAPES (PNPD 1797079), FAPESP (2014/50279-4) for financial support, and Professor Dr. Tiago Venâncio (Department of Chemistry-UFSCar) for the ^{27}Al-NMR experiments.

Declarations

Conflict of interest The authors declare that there is no conflict of interest.

References

Abdullah B, Abd Ghani NA, Vo DVN (2017) Recent advances in dry reforming of methane over Ni-based catalysts. J Clean Prod 162:70–185

Agencia Iberoamericana para diffusion de la Ciencia y la Tecnologia. https://www.dicyt.com. Accessed 2020.

Al-Mubaddel FS, Kumar R, Sofiu ML, Frusteri F, Ibrahim AA, Srivastava VK, Kasim SO, Fakkeha AH, Abasaeed AH, Osman AI, Al-Fatesh AS (2021) Optimizing acido-basic profile of support in Ni supported La_2O_3+Al_2O_3 catalyst for dry reforming of methane. Int J Hydrog Energy 46:14225–14235

Alsaffar MA, Ayodele BV, Ali JM, Ghany MAA, Mustapa SI, Cheng CK (2021) Kinetic modeling and reaction pathways for thermocatalytic conversion of carbon dioxide and methane to hydrogen-rich syngas over alpha-alumina supported cobalt catalyst. Int J Hydrog Energy 46:30871–30881

Anjaneyulu C, Kumar VV, Bhargava SK, Venugopal A (2013) Characteristics of La-modified Ni-Al_2O_3 and Ni-SiO_2 catalysts for CO_x-free hydrogen production by catalytic decomposition of methane. J Energy Chem 22:853–860

Bartholomew CH, Farrauto RJ (2006) Fundamentals of industrial catalytic processes, 2nd edn. Wiley, New York

Bertoldi J, Roseno KTC, Schimal M, Lage VD, Lenzi GG, Brackmann R (2022) $La_{1-x}(Ce, Sr)_xNiO_3$ perovskite-type oxides as catalyst precursors to syngas production through tri-reforming of methane. Int J H2 Energy 47:31279–31294

Brasil Energia: Petróleo&Gás. 33, 408 (2014).

Chein RY, Wang CY, Yu CT (2017) Parametric study on catalytic tri-reforming of methane for syngas production. Energy 118:1–17

Christensen KO, Chen D, Lödeng R, Holmen A (2006) Effect of supports and Ni crystal size on carbon formation and sintering during steam methane reforming. Appl Catal Gen 314:9–22

Cichy M, Pánczyk M, Slowik G, Zawadzki W, Borowiecki T (2022) Ni–Re alloy catalysts on Al_2O_3 for methane dry reforming. Int J Hydrog Energy 47:165828–216543

Cui Y, Zhang H, Xu H, Li W (2007) The CO_2 reforming of CH_4 over Ni/La_2O_3/α-Al_2O_3 catalysts: the effect of La_2O_3 contents on the kinetic performance. Appl Catal A Gen 331:60–69

Damyanova S, Perez CA, Schmal M, Bueno JMC (2002) Characterization of ceria-coated alumina carrier. Appl Catal A Gen 234:271–282

Farniaei M, Abbasi M, Rahnama M, Rahimpour MR, Shariati A (2014) Syngas production in a novel methane dry reformer by utilizing of tri-reforming process for energy supplying: modeling and simulation. J Nat Gas Sci Eng 20:132–146

Gao J, Hou Z, Guo J, Zhu Y, Zheng X (2008) Catalytic conversion of methane and CO_2 to synthesis gas over a La_2O_3-modified SiO_2 supported Ni catalyst in fluidized-bed reactor. Catal Today 131:278–284

García-Vargas JM, Valverde JL, Dorado F, Sánchez P (2014) Influence of the support on the catalytic behaviour of Ni catalysts for the dry reforming reaction and the tri-reforming process. J Mol Catal A Chem 395:108–116

GasNet (2020) O Site do Gás Natural e GNV. https://www.gasnet.com.br. Accessed 2020

Guo W, Li G, Zheng Y, Li K, Guo L (2022) Influence of La_2O_3 addition on activity and coke formation over Ni/SiO_2 for acetic acid steam reforming. Int J Hydrog Energy 47:3633–3643

Gupta S, Deo G (2023) Effect of metal amount on the catalytic performance of Ni–Al_2O_3 catalyst for the Tri-reforming of methane. Int J Hydrog Energy 48:5478–5492

Habibi N, Rezaei M, Majidian N, Andache M (2014) CH_4 reforming with CO_2 for syngas production over La_2O_3 promoted Ni catalysts supported on mesoporous nanostructured γ-Al_2O_3. J Energy Chem 23:435–442

Izquierdo U, Barrio VL, Requies J, Cambra JF, Güemez MB, Arias PL (2014) Tri-reforming: a new biogas process for synthesis gas and hydrogen production. Int J Hydrog Energy 38:7623–7631

Jun KW, Roh HS, Kim KS, Ryu JS, Lee KW (2004) Catalytic investigation for Fischer–Tropsch synthesis from bio-mass derived syngas. Appl Catal A Gen 259:221–226

Kalai DY, Stangeland K, Jin Y, Tucho WM, Yu Z (2018) Biogas dry reforming for syngas production on La promoted hydrotalcite-derived Ni catalysts. Int J Hydrog Energy 43:19438–19450

Kang JS, Kim DH, Lee SD, Hong SI, Moon DJ (2007) Nickel-based tri-reforming catalyst for the production of synthesis gas. Appl Catal A Gen 332:153–158

Kumar R, Pant KK (2020) Hydrotalcite-derived Ni-Zn-Mg-Al catalyst for Tri-reforming of methane: effect of divalent to trivalent metal ratio and Ni loading. Fuel Process Technol 210:106559

Kumar A, Mukasyan AS, Wolf EE (2011) Combustion synthesis of Ni, Fe and Cu multi-component catalysts for hydrogen production from ethanol reforming. Appl Catal A Gen 401:20–28

Kumar R, Kumar K, Choudary NV, Pant KK (2019) Effect of support materials on the performance of Ni-based catalysts in tri-reforming of methane. Fuel Process Technol 186:40–52

Kumar KDPL, Naidu BN, Sarkar B, Mondal P, Ghosh K, Prasad VVDN (2021) Enhanced CO_2 utilization via methane tri-reforming over Ru incorporated Co/MgO-Al_2O_3 catalyst: Influence of La and Ce promoters. J Environ Chem Eng 9:105949

Li B, Watanabe R, Maruyama K, Kunimori K, Tomishige K (2005) Thermographical observation of catalyst bed temperature in oxidative steam reforming of methane over Ni supported on α-alumina granules: effect of Ni precursors. Catal Today 104:7–17

Lino AVP, Calderon YNC, Mastelaro VR, Assaf EM, Assaf JM (2019) Syngas for Fischer–Tropsch synthesis by methane tri-reforming using nickel supported on $MgAl_2O_4$ promoted with Zr, Ce and Ce-Zr. Appl Surf Sci 481:747–760

Lino AVP, Assaf EM, Assaf JM (2020a) Adjusting process variables in methane tri-reforming to achieve suitable syngas quality and low coke deposition. Energy Fuels 34:16522–16531. https://doi.org/10.1021/acs.energyfuels.0c02895

Lino AVP, Rodella CB, Assaf EM, Assaf JM (2020b) Methane tri-reforming for synthesis gas production using Ni/$CeZrO_2$/$MgAl_2O_4$ catalysts: effect of Zr/Ce molar ratio. Int J Hydrog Energy 45:8418–8432

Majewski AJ, Wood J (2014) Tri-reforming of methane over Ni@SiO_2 catalyst. Int J Hydrog Energy 39:12578–12585

Osat M, Shojaati F (2022) Assessing performance of methane tri-reforming reactor using a parametric study on the fundamental process variables. Clean Chem Eng 3:100050

Osat M, Shojaati F, Hafizi A (2022) Optimization and improvement of a conventional tri-reforming reactor to an energy efficient membrane reactor for hydrogen production. Chem Eng Process 175:108933

Özdemir H, Faruk Öksüzömer MA, Gürkaynak MA (2014) Effect of the calcination temperature on Ni/$MgAl_2O_4$ catalyst structure and catalytic properties for partial oxidation of methane. Fuel 116:63–70

Pompeo F, Nichio NN, Souza MMVM, Cesar DV, Ferretti OA, Schmal M (2007) Study of Ni and Pt catalysts supported on α-Al_2O_3 and ZrO_2 applied in methane reforming with CO_2. Appl Catal A 316:175–183

Pompeo F, Gazzoli D, Nichio NN (2009) Stability improvements of Ni/α-Al_2O_3 catalysts to obtain hydrogen from methane reforming. Int J Hydrog Energy 34:2260–2268

Shi L, Deng GM, Li WC, Miao S, Wang QN, Zhang WP, Lu AH (2015) Al_2O_3 nanosheets rich in pentacoordinate Al^{3+} ions stabilize Pt-Sn clusters for propane dehydrogenation. Angew Chem 54:13994–13998. https://doi.org/10.1002/anie.201507119

Song C, Pan W (2004) Tri-reforming of methane: a novel concept for catalytic production of industrially useful synthesis gas with desired H_2/CO ratios. Catal Today 98:463–484

Song JH, Yoo S, Yoo J, Park S, Gim MY, Kim TH, Song IK (2017) Hydrogen production by steam reforming of ethanol over Ni/Al_2O_3–La_2O_3 xerogel catalysts. Mol Catal 434:123–133

Świrk K, Grams J, Motak M, da Costa P, Grzybek T (2020) Understanding of tri-reforming of methane over Ni/Mg/Al hydrotalcite-derived catalyst for CO_2 utilization from flue gases from natural gas-fired power plants. J CO2 Util 42:10317

Thyssen VV, Assaf EM (2014) Ni/La_2O_3–SiO_2 catalysts applied in glycerol steam reforming reaction: effect of the preparation method. J Braz Chem Soc 25:2455–2465

Thyssen VV, Maia TA, Assaf EM (2013) Ni supported on La_2O_3–SiO_2 used to catalyze glycerol steam reforming. Fuel 105:358–363

Thyssen VV, Maia TA, Assaf EM (2015) Cu and Ni catalysts supported on γ-Al_2O_3 and SiO_2 assessed in glycerol steam reforming reaction. J Braz Chem Soc 26:22–31

Thyssen VV, Georgetti F, Assaf EM (2017a) Influence of MgO content as an additive on the performance of Ni/MgO–SiO_2 catalysts for the steam reforming of glycerol. Int J Hydrogen Energy 42:16979–16990

Thyssen VV, Nogueira FGE, Assaf EM (2017b) Study of the influence of nickel content and reaction temperature on glycerol steam reforming with Ni/La_2O_3–SiO_2 catalysts. Int J Res Eng Sci 5:54–62

Thyssen VV, Sartore DM, Assaf EM (2019) Effect of preparation method on the performance of Ni/MgO–SiO_2 catalysts for glycerol steam reforming. J Energy Inst 92:947–958

Trimm DL (1999) Catalysts for the control of coking during steam reforming. Catal Today 49:3–10

Tsiotsias AI, Charisiou ND, Sebastian V, Gaber S, Hinder SJ, Baker MA, Polychronopoulou K, Goula MA (2021) A comparative study of Ni catalysts supported on Al_2O_3, MgO–CaO–Al_2O_3 and La_2O_3–Al_2O_3 for the dry reforming of ethane. Int J Hydrog Energy 47:5337–5353

Vilela VB, Thyssen VV, Rodrigues LN, Fonseca FC (2021) Enhancing the catalytic activity of lanthanum-ceria fluorite for methane conversion in SOFC. ECS Trans 103:1917–1925

Vita A, Pino L, Cipitì F, Laganà M, Recupero V (2014) Biogas as renewable raw material for syngas production by tri-reforming process over $NiCeO_2$ catalysts: optimal operative condition and effect of nickel content. Fuel Process Technol 127:47–58